Numerical Experiments with Large-Scale Seasonal Forcing[1]

E. B. KRAUS

Woods Hole Oceanographic Institution, Woods Hole, Mass.

AND E. N. LORENZ

Massachusetts Institute of Technology, Cambridge, Mass.

(Manuscript received 26 August 1965)

ABSTRACT

Experiments with six different heating fields in a numerical general circulation model are described. Three different vertical heating gradients are each used once with and once without variations on the continental-oceanic scale along parallel circles. The zonal and the meridional heating fields are forced to vary seasonally. Integration has been carried out over a simulated period of one century for one particular configuration, and over periods of five years for each of the five other configurations.

Results which may be represented by an electrical analogue are rather similar to actual general circulation observations. They also show stronger summer westerlies and North-South temperature gradients in the model without schematic oceans and continents. Dynamic lag effects cause differences between the "climates" of spring and fall. In all experiments there was a breakdown in fall of a predominantly zonal circulation, accompanied by the development of "equinoctial storms."

Lag correlations computed for the mean zonal thermal wind in the 100-year experiment show persistence in summer between successive ten-day means and significant negative values over longer lag periods. No significant lag correlations were found during the winter months.

1. Introduction

In an earlier paper (1963) we related changes in the vertical heating gradient to the fields of temperature and motion that could be generated in a simple numerical model of a general circulation. The forcing was proportional to the difference between the actual potential temperature $\theta(x,y,p)$ and a "thermal equilibrium" potential temperature $\theta^*(x,y,p)$ which would ultimately prevail if there were no motion. Our model was restricted to two layers, and we studied the circulation patterns associated with three different values of the difference between the horizontal means of θ^* in the upper and lower layers, i.e., of three different thermal-equilibrium vertical temperature gradients σ^*.

The differences between the resulting circulation patterns were compatible with the rather incomplete knowledge which is available about actual differences between circulation patterns associated with different climatic regimes. It was concluded, therefore, that the latter differences could have been produced conceivably by changes in the vertical heating rate. Any change in the mean atmospheric mixing ratios of O_3, CO_2, or H_2O could be expected to affect primarily the vertical heating gradient.

The quoted study made no allowance for seasonal variations in the forcing functions. These variations have now been introduced. We have integrated the model with one particular configuration, in which the variations of the forcing with latitude and longitude are themselves variable with the season, over a simulated period of 100 years real time. The output provides a set of data which may be used later to learn something about such things as variability and predictability in different seasons. In the present paper, these 100 years' data provide the basis for the lag correlations discussed below. In addition, we have integrated the model for a simulated period of five years with each of three different values of σ^*, both with and without longitudinally variable forcing. This represents a set of six different configurations.

Comparison shows that the temperature difference between the northern and southern boundaries of the model, as well as the mean westerly wind speed, tends to be less when the forcing varies with longitude than when it does not. This applies particularly during the "summer" of the model when the meridional heating gradient is weak. The reduced temperature difference is due to the meridional heat transport by standing, monsoon-type circulations which form on a continental scale as a direct result of the forcing. The meridional temperature difference and the associated zonal thermal wind are larger when there is no such heat transport by standing circulations. The difference is not unlike that which is actually observed between the Northern Hemisphere, where heating differences within zones are more pronounced, and the more symmetric Southern Hemisphere.

[1] Contribution No. 1703 of the Woods Hole Oceanographic Institution.

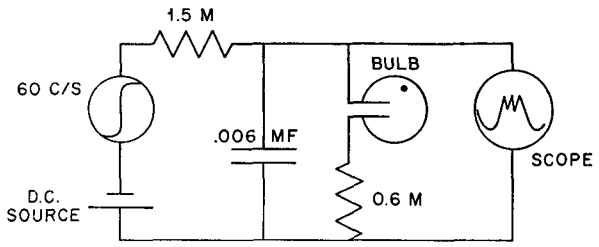

FIG. 1. Electric analog circuit.

Krueger, Winston and Haines (1965) found that the year-to-year variability of the zonal available potential energy in the actual atmosphere was much larger during the autumn buildup than during the spring decline. The conversion between eddy and zonal energy was also found to be much larger in October than in April during the period studied by Wiin-Nielson, Brown and Drake (1964). In general the state of the atmosphere exhibits seasonally asymmetrical variations which characteristically lag a month or more behind the seasonal solar cycle. The thermal capacity of the sea and, to a lesser extent, that of the soil and the air, must contribute to this lag and may be its virtual cause. The possibility can be considered, however, that the dynamics of the system itself will necessarily involve phase shifts from the forcing function. The meridional heating gradient is larger in winter than in summer. As it increases during fall the mean zonal thermal wind becomes stronger. This, in turn, favors the development of baroclinic perturbations which can transport heat toward the poles and so check or temporarily reverse the seasonal increase of the meridional temperature difference and of the associated thermal wind. The development of baroclinic perturbations to the stage where they can contribute to the meridional heat flux requires a finite lapse of time. As a result, the meridional temperature difference cannot be in phase with the meridional heating gradient.

In an analogy with a simple electrical experiment which we have set up, the heating difference between the equator and the poles corresponds to an applied (seasonally variable) potential. The zonal thermal wind then becomes the charge on a capacitor, while a baroclinic perturbation is simulated by a neon bulb which requires a critical voltage before it begins to operate, but which will then conduct current rather efficiently. The meridional temperature contrast or the mean strength of the westerlies may then be compared with the output voltage from a simple network made of these elements (Fig. 1). An oscilloscope photograph of this output is shown as Fig. 2. In this case, we simply used 60-cycle alternating current to simulate the "seasonally" variable input potential.

The oscillograph is suggestively similar to the plot of zonal available potential energy in the atmosphere shown in Fig. 3. It is even more similar to the corresponding output from our model as shown in Figs. 5, 6 and 7 below. The analogy could be taken further by simulating the effect of the standing, monsoon-type circulation with a variable leakage across our capacitor, which would be most effective when the input voltage is close to its highest or lowest value (solstices) and which would be zero at some intermediate time (equinoxes). This would result in a lowering of the output voltage (westerlies) at the time when the input wave is close to its vertices (solstices). At the intermediate time, the ouput potential will build up rapidly and fluctuate rather vigorously (equinoctial storms). All these features are observed, in fact, in our model, though it would be misleading to take the analogies too far. There are essential differences between the action of a neon bulb and that of a baroclinic disturbance. Our numerical model is considerably more complex than the network in Fig. 1. The real atmosphere, in turn, is far more complex than the simple model which forms the topic of this paper.

2. The model

The present paper is based on the same two-layer model (Lorenz, 1960) which formed the basis of our preceding paper. A description of the spectral form of this model and of the integration method may be found in that paper or in later publications (Lorenz, 1965).

In the upper layer of the model, the stream function for the nondivergent part of the horizontal flow is

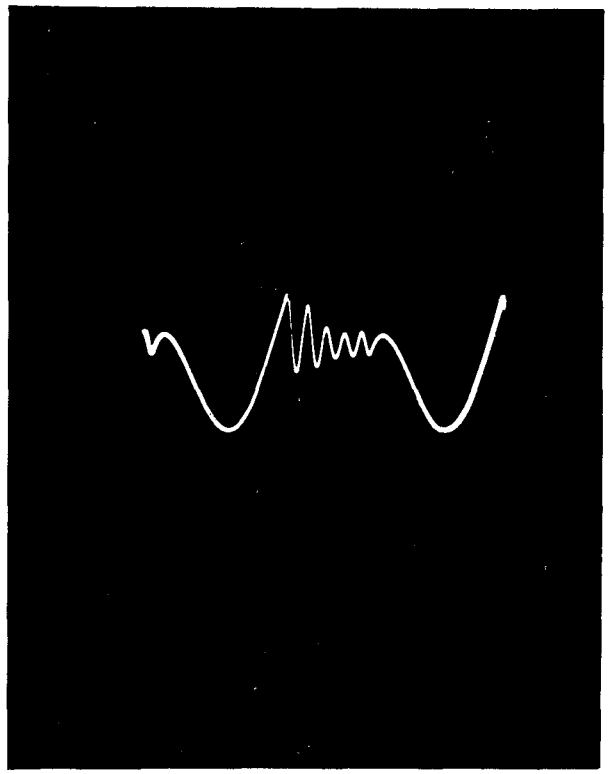

FIG. 2. Oscilloscope display of electric analog.

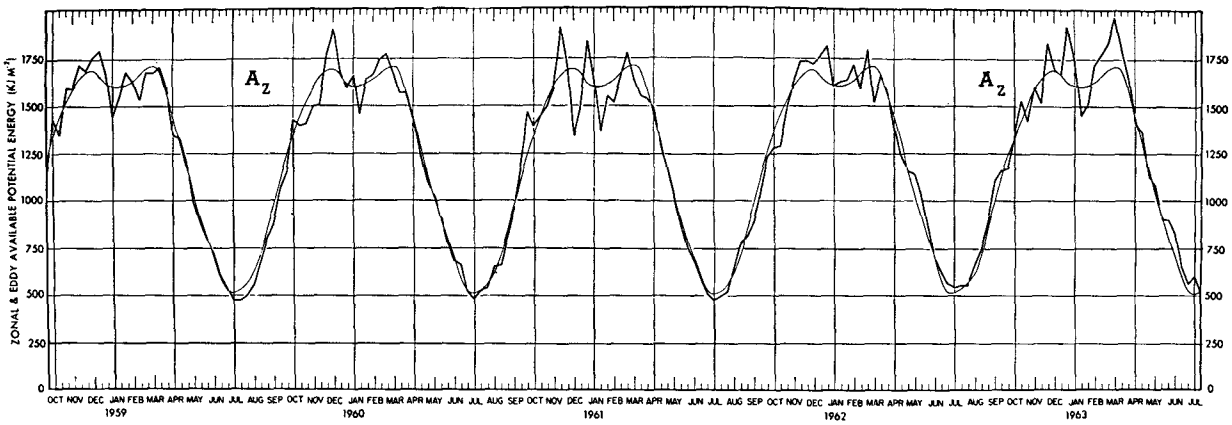

FIG. 3. Variation of 10-day averages of zonal available potential energy for the layer 850–500 mb (heavy curve) for the period October 1958–July 1963. The light curve is the same for each year and represents averages of the monthly values for the five years of data (after Krueger, Winston and Haines, 1965).

denoted by $\psi+\tau$, the velocity potential for the non-rotational part by χ, and the potential temperature by $\theta+\sigma$. The corresponding fields in the lower layer are denoted by $\psi-\tau$, χ and $\theta-\sigma$. Horizontal variations of σ and of the coriolis parameter f are excluded. The resulting set of equations has the form:

$$\frac{\partial}{\partial t}\nabla^2\psi=-J(\psi,\nabla^2\psi)-J(\tau,\nabla^2\tau)+N(\psi), \tag{1}$$

$$\frac{\partial}{\partial t}\nabla^2\tau=-J(\psi,\nabla^2\tau)-J(\tau,\nabla^2\psi)+f\nabla^2\chi+N(\tau), \tag{2}$$

$$\frac{\partial}{\partial t}\theta=-J(\psi,\theta)+\sigma\nabla^2\chi+N(\theta), \tag{3}$$

$$\frac{\partial}{\partial t}\sigma=\nabla\theta\cdot\nabla\chi+N(\sigma), \tag{4}$$

$$\nabla^2(\tau/S_\psi-\theta/S_\theta)=0. \tag{5}$$

The dimensional proportionality constants in the thermal wind equation (5) are defined by:

$$S_\psi=a^2f,$$

where a is a characteristic horizontal scale length, and by

$$S_\theta=\frac{2a^2f^2p_0{}^\kappa}{c_p(p_1{}^\kappa-p_3{}^\kappa)},$$

where p_0, p_1, p_3 are the pressures at the lower boundary and in the middle of the two layers.

Friction and heating are represented by the linear terms

$$N(\psi)=-k\nabla^2(\psi-\tau), \tag{6}$$

$$N(\tau)=k\nabla^2(\psi-\tau)-K\nabla^2\tau, \tag{7}$$

$$N(\theta)=-(j+b)(\theta-\theta^*)+h(\sigma-\sigma^*), \tag{8}$$

$$N(\sigma)=h(\theta-\theta^*)-(j+b)(\sigma-\sigma^*)-H(\sigma-\sigma_c). \tag{9}$$

The coefficients in these expressions have all the dimensions of inverse time; $2k$ and K are friction coefficients at the lower surface and the surface separating the two layers; $2h$ represents the rate of radiational and frictional heating at the lower boundary; j the rate of radiational heating in the interior. The last term in (9) requires some explanation. Vertical mixing in dry air would tend to produce a uniform potential temperature; that means it would tend to drive the stability parameter toward zero. In the actual atmosphere the establishment of such a dry-adiabatic lapse rate tends to be inhibited by condensation. In the present model it has therefore been assumed that convection drives the vertical stability not towards zero but towards some larger critical value.

To solve Eqs. (1)–(5), the dependent variables as well as the prescribed field of θ^* are expressed in spectral form, with the usual summation convention, by functions of the type

$$G=S_G[G_{nm}(t)F_{nm}(x,y)+G_{nm}{}'(t)F_{nm}{}'(x,y)]. \tag{10}$$

The sets of orthogonal functions F and F' are characterized by the relations:

$$\overline{F_{ij}F_{kl}}=\delta_{ik}\delta_{jl}, \tag{11}$$

$$\nabla^2F_{ij}=-\frac{i^2+j^2}{a^2}F_{ij}, \tag{12}$$

where the bar denotes a horizontal average and a is the horizontal scale length. At the boundary the tangential derivative

$$\frac{\partial F_{ij}}{\partial s}=0, \tag{13}$$

and the functions G_{nm} and G_{nm}' have the character of time dependent amplitudes.

As in earlier papers, our geometry is an infinite channel of width πa. The x and y axes are directed along and across the channel. The set of spectral functions

$$\begin{aligned} F_{nm} &= 1 && \text{for } n=0 \quad m=0 \\ &= \sqrt{2}\cos my/a && \text{for } n=0 \quad m>0 \\ &= 2\sin my/a \cos nx/a && \text{for } n>0 \quad m>0 \\ F_{nm}' &= 2\sin my/a \sin nx/a && \text{for } n>0 \quad m>0, \end{aligned} \tag{14}$$

satisfies the conditions (11), (12), and (13). It can be readily seen that the amplitudes of F_{00} have no effect on the behavior of the remaining variables. We have further simplified the problem by omitting the interactions between different wave numbers (products of two orthogonal functions with two different non-zero values of n), while the interaction of each wave with the zonal current is retained.

3. Specific scales and parameters

In the geometry of the present study, the thirtieth parallel is supposed to bisect the area between the two

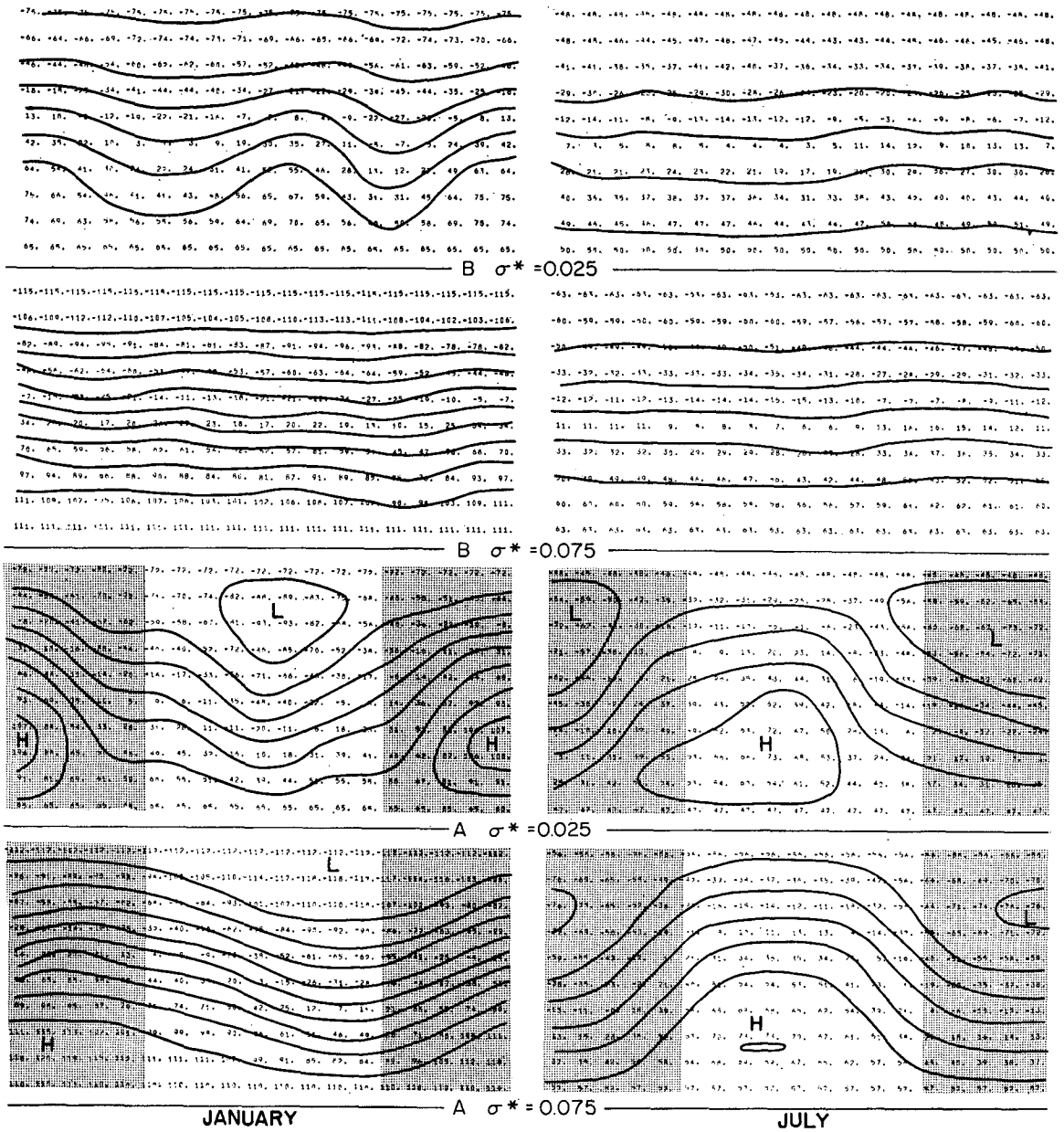

FIG. 4. January and July averages of the mean flow stream function ψ for two values of the forcing parameter τ^*. Continents in Model A are shaded.

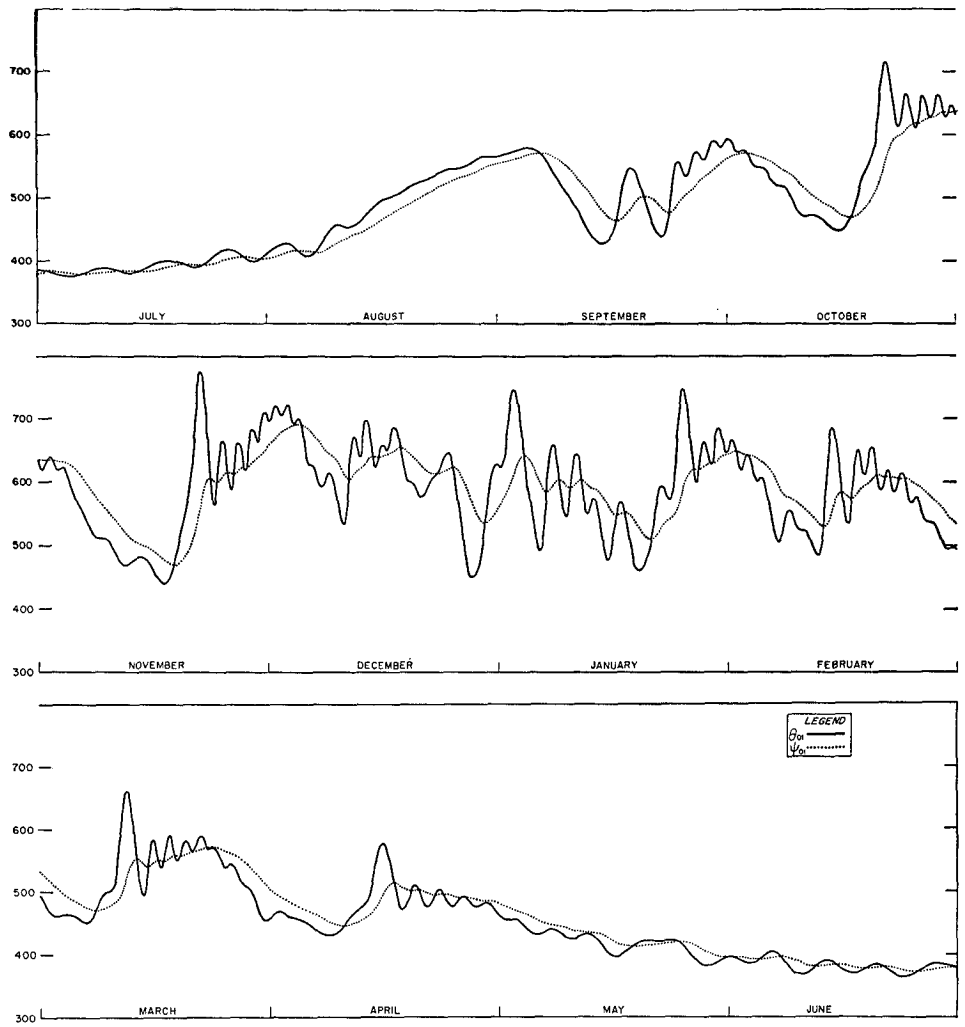

FIG. 5. Values of the mean westerly flow ψ_{01} and of the mean zonal thermal wind θ_{01} during one year of record.

latitudinal boundary walls. The length of this parallel is about 34,800 km. We assume a cyclical repetition of the motion every 120° of longitude or every 11,600 km, which is double the distance between the latitudinal walls. Our scale length

$$a = 11{,}600/2\pi = 1{,}846 \text{ km}.$$

For our time unit we chose the reciprocal value of the coriolis parameter at 30° latitude:

$$f(30°) = 7.29 \times 10^{-5} \text{ sec}^{-1} = (3.81 \text{ hours})^{-1}.$$

The same unit was also chosen for the time increment in the numerical integrations. This unit is approximately four hours and we have for convenience chosen six time increments as our day; likewise, we have let our year consist of twelve 30-day months, with the solstices occurring on 1 January and 1 July.

Assuming $p_0/p_1/p_3 = 1000/750/250$, our temperature scale is defined by

$$S_\theta = 146\text{C}.$$

The frictional and heating coefficients have dimensions of inverse time and can therefore be expressed as multiples of f. We chose $k=j=h=3f/64$ and $K=H=3f/128$. These values are $\frac{3}{4}$ of those used previously. The critical stability $\sigma_c = 10\text{C}$ or 0.0685 in nondimensional units as before.

The sequence of spectral functions is truncated so that $m \leqslant 2$ and $n \leqslant 4$. All references to F_{nm} or F_{nm}' for larger n and m are omitted from the computation. This truncation is partly justified by the small amplitude that is, in fact, observed in our numerical output for the highest retained wave number $n=4$, which corresponds to wave number 12 on the planetary scale.

We have specified two different horizontal distributions for the thermal equilibrium temperature θ^* with

the following values of the amplitudes θ^*_{nm} and θ'^*_{nm} where "season" is defined as cos $(2\pi t/\text{year})$.

Model A	Model B
$\theta_{00}^* = -0.0623$ season	$\theta_{00}^* = -0.623$ season
$\theta_{01}^* = 0.088 + 0.044$ season	$\theta_{01}^* = 0.088 + 0.044$ season
$\theta_{11}'^* = 0.022$ season	$\theta_{11}'^* = 0.0$
$\theta_{31}'^* = 0.073$ season	$\theta_{31}'^* = 0.0$

$\theta_{11}^* = \theta_{12}'^* = \theta_{21}^* = \theta_{22}'^* = \theta_{31}^* = \theta_{32}'^* = \theta_{41}^* = \theta_{42}'^* = 0.001$
$\theta_{02}^* = \theta_{12}^* = \theta_{21}'^* = \theta_{22}^* = \theta_{32}^* = \theta_{41}'^* = \theta_{42}^* = 0.0$

Model B is free of heating differences along the circles of latitude (except for the quantities listed which have the very small value 0.001) and may be compared to a sea-covered hemisphere. In model A the terms $\theta_{11}'^*$ and $\theta_{31}'^*$ provide a heating function which varies with season and longitude. In contrast to actual conditions and to our earlier model, the regions of cooling and heating (oceans and continents) are assumed to be of equal width. This was done to test the effect of different combinations of meridional and zonal heating gradients with a minimum of irrelevant additional complications. The constant, non-zero value (0.001) for the amplitude of each available wave number and mode which is not subject to seasonal variation was introduced to increase the "noise level" of the experiment and to prevent unforced wave numbers from dying out altogether.

The prescribed values for σ^* are 0.025, 0.050 and 0.075, corresponding to dimensional thermal equilibrium, potential temperature differences of 7.3, 14.6 and 21.9C between the upper and lower layers. Applied to models A and B this gives the six different configurations.

Sample mean monthly charts, based on the five years simulated data are shown in Fig. 4. The evolution during one particular year of the amplitudes ψ_{01} and θ_{01} for the mean geodynamic height difference and the mean potential temperature difference between the latitudinal boundaries are shown in Fig. 5 for Model A with $\sigma^* = 0.050$.

4. Comparison between different configurations

The zonal available potential energy computed by Kreuger *et al.* (1965) depends non-linearly on the

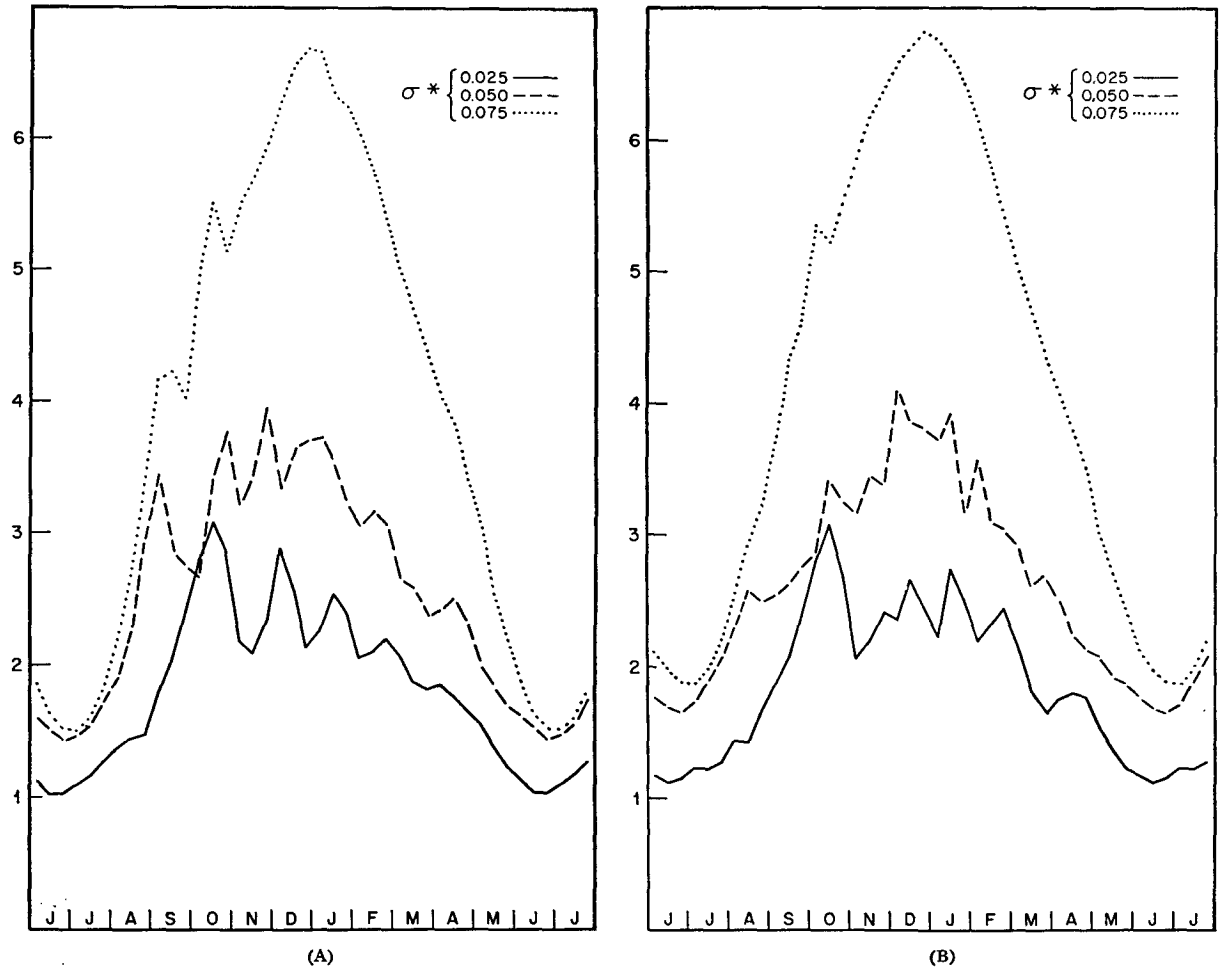

FIG. 6. Ten day means of the sum of squares of θ_{01} averaged over five years of record with different values of σ^*; A, with forcing along parallel circles and B, without forcing along parallel circles.

TABLE 1. Five-year averages of mean meridional westerly windflow (m sec^{-1}) and mean potential temperature difference (°K) between meridional boundaries in July for various values of σ^*.

	σ^* 0.075	0.050	0.025
	Windflow		
Model A	4.8	4.7	4.0
Model B	5.4	5.2	4.2
	Temperature		
Model A	16.6	16.4	14.1
Model B	18.6	18.0	14.5

temperature variance within the isobaric layers and on the vertical stability. We did not produce an output of this quantity, though it could be readily computed from our tapes. We did produce an output of the kinetic energy of the mean zonal thermal wind, which is closely related to the zonal available potential energy. Its seasonal march is plotted in Figs. 6a and 6b.

The figures show that the effect of continents and oceans, that is of variable heating along parallel circles, is much less conspicuous in our computations than the effect of changes in σ^*. Examination of the vertical scale indicates, however, that the energy of the westerly wind shear and, by the same token, of the north-south temperature difference during summer, is considerably higher when there is no forcing within zones, particularly for the more stable configurations. Mean westerly velocities are also larger on a zonally uniform planet. Averages for July in dimensional units are shown in Table 1.

The difference between the two models is due to the role of the standing monsoon-type circulations which are forced in Model A by the zonal heating pattern. These quasi-stationary circulations can transport heat toward the poles. That reduces the meridional temperature gradient. The difference between the two models is not unlike that between the real northern and southern hemispheres. The latter, zonally more uniform, is characterized also by stronger meridional temperature gradients and stronger summer westerlies. The existence or absence of pronounced heating gradients along parallel circles may not be the only cause of the difference between the hemispheres, but it is probably a contributory cause.

The meridional temperature gradient and the mean westerlies remain stronger in the model with zonally uniform forcing through most of the year. The only exception is a relatively short period in fall. At the end of summer the zonal forcing also becomes zero in Model A. The meridional heat transport by the standing circulation vanishes and the meridional temperature gradient develops significantly before traveling perturbations develop sufficiently to carry the poleward flux of heat. This lag effect will be discussed further below.

The annual march of the stability σ is very similar in the two models. In Fig. 7 it is illustrated for Model B. The forcing function does not vary with time and is marked by the horizontal lines in the figure. The mean vertical heating gradient $N(\sigma)$ as defined in Eq. (9) is smaller at any time of the year for larger σ^*. In fact, for the most stable model ($\sigma^*=0.075$), the vertical forcing is reversed for the two months during summer. The upper layer is then heated while the lower is cooled. The circulation in this model during this period has almost entirely the character of a Hadley regime.

The variation of the kinetic energy

$$E=\sum_n \sum_m E_{nm} \propto \sum_n \sum_m (n^2+m^2) \times (\psi_{nm}^2+\psi_{nm}'^2+\theta_{nm}^2+\theta_{nm}'^2)$$

between the different configurations at any time of the year is small compared to its annual variation, in spite of the large difference in the vertical heating. On the other hand the distribution of the kinetic energy between the various wave numbers is very strongly affected by differences in vertical or zonal forcing. This is demonstrated by the graphs of the kinetic energy weighted mean wave number

$$\bar{N}=\sum_n \sum_m nE_{nm}/E$$

in Fig. 8. The most striking aspect of Fig. 8 is the apparent reversal of the seasonal variation: the mean wave number reaches its lowest value in summer for

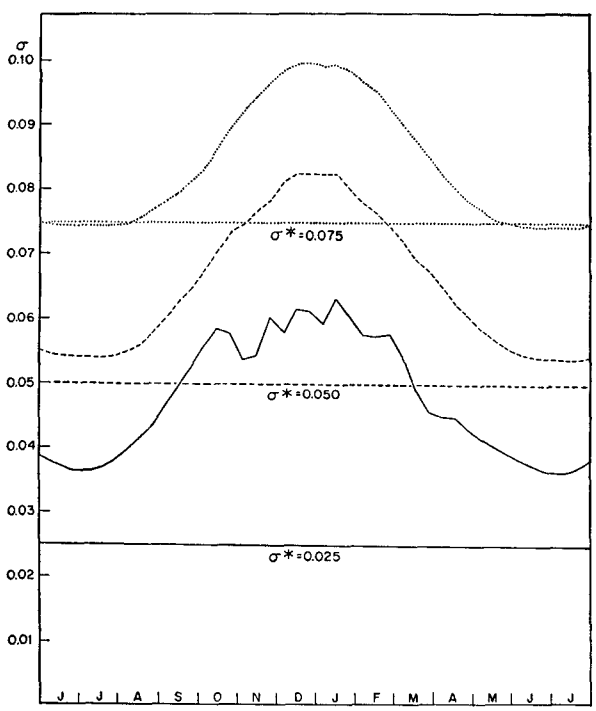

FIG. 7. Ten day means of the vertical stability σ in Model B for different values of the forcing function σ^*.

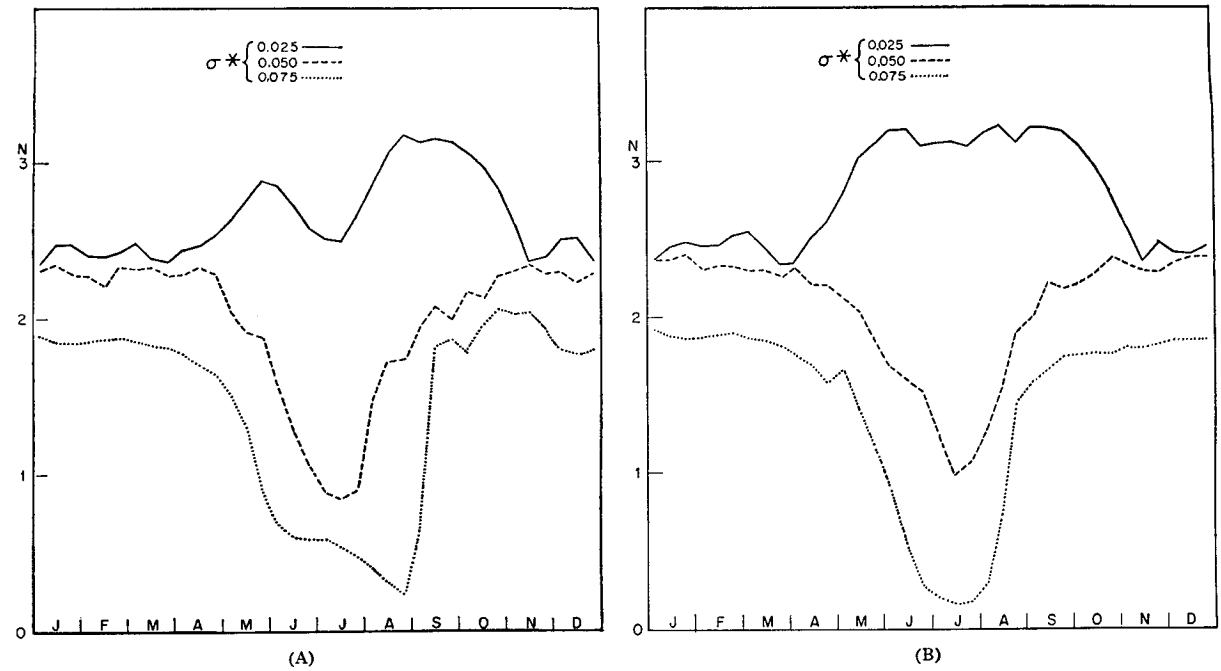

FIG. 8. Annual variation of the kinetic-energy-weighted mean wave number $\bar{N}$; A, with forcing along parallel circles, and B, without forcing along parallel circles.

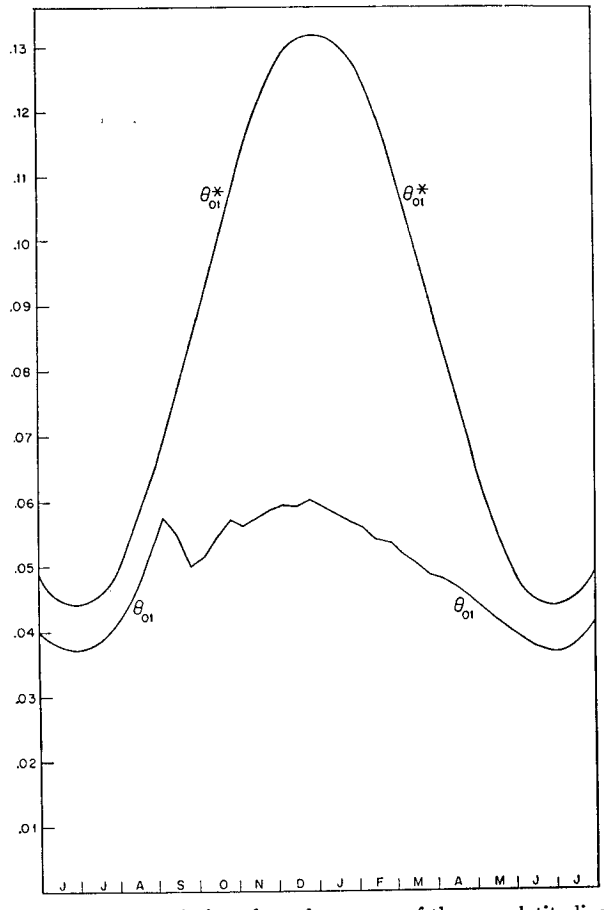

FIG. 9. Annual variation of ten day means of the cross-latitudinal forcing term θ_{01}^* and of the hundred year average of θ_{01}.

$\sigma^*=0.050$ or 0.075 with high values in summer for $\sigma^*=0.025$. This reversal is due to our including the zonal flow and the associated Hadley circulation (wave number 0) in the calculation of $\bar{N}$. In the absence of continental oceanic heating, the flow during summer is mainly zonal in the models characterized by the two higher values of σ^*. With continental oceanic heating, the flow is dominated by wave number 1. The unforced, dynamically generated perturbations, however, tend to have their lowest wave numbers during winter when the actual static stability is greatest in all three configurations, in agreement with accepted theory.

In summer, wave number 1 is forced strongly in Model A, and that causes the more complicated annual variation shown by the figure. The forcing of wave number 1 is of course equally strong in winter, but it is then less effective because of the greater mean cross-latitude forcing.

Wave number 3 also is forced in Model A, but this wave has actually more energy without zonal forcing. On the average the shorter waves tend to move faster from west to east. This means that the energy of wave 3 will be alternately increased and decreased by the same wave number component of the fixed forcing function θ^*. The mean energy of wave number 3 is little affected by the zonal forcing in these circumstances. It will depend mainly on the meridional gradient and this appears more conducive for the development in Model B.

5. The dynamic lag

The forcing functions for all six configurations are symmetric in time. When plotted, the period July-

December would appear as a mirror image of the period January-June. By contrast, the graphs in Fig. 8 are all asymmetric with a pronounced lag in the summer vertices behind the vertices of the forcing function.

In Fig. 9 we have plotted both θ_{01}^* and the 10-day mean (averaged over 100 years) of θ_{01} for Model A with $\sigma^*=0.050$. It can be seen that the graph of θ_{01} follows the equilibrium temperature θ_{01}^* closely during summer; it then breaks suddenly away to follow a course during fall which is quite different from that shown for spring.

Fig. 9 is similar in character to Figs. 3, 5 and 6. Most of the peaks and troughs in the annual march of θ_{01} which are shown in Fig. 5 are smoothed out in the 100-year average of 10-day means. Some remain, however, notably the break-off in fall and the first subsequent peak. There is an analogue for this in the real atmosphere, where certain phenomena also tend to occur on statistically preferred calendar dates. The breakdown of the stratospheric polar night vortex falls into this category as does the occurrence of cold air outbreaks over Europe on certain days of May which entered as the "ice saints" into folk weather lore.

The time delay in our electrical analogue must increase with the capacity of the condenser. In the dynamic system, the zonal thermal wind plays the role of a capacitor. It balances a meridional temperature gradient, and therefore represents a reservoir of available potential energy and of "available kinetic energy" of the shearing motion. With other conditions equal, the characteristic time delay must increase with the energy storage capacity of this reservoir. This capacity would be reduced by a more intense momentum exchange between the two layers in our model, that is, by larger values of k. The time lag is affected, however, not only by the thermal wind but also by the threshold characteristics for the development of the different wave numbers, by the heat transfer coefficients, and by the heat flux. It cannot be expressed therefore simply by the linear resonance period of Eqs. (1) and (2) which would have a constant value of $2\pi/\sqrt{kK}$ or about 22 days.

6. Persistence

Persistence at various time lags is a notable feature of real atmospheric behavior. An extended-range forecasting scheme based upon persistence often shows positive skill (if a forecast of the climatological normal is chosen as a basis for comparison) when more sophisticated methods seem to fail. In order to study persistence in our model we have used our 100-year data sample.

The variable whose persistence we have studied is θ_{01}. From the complete set of 216,000 instantaneous values of θ_{01} we have formed 3600 non-overlapping 10-day means. These 3600 values were arranged as 36 separate time series, one for each calendar 10-day period, with 100 "observations" in each series.

Correlations between these series were then determined, at lags ranging from 10 to 360 days (the separate series are therefore correlated at lags of 0 or 1 observations). To avoid a possible transient effect due to the choice of initial conditions, the first six months of the 100-year sample were not used. For certain correlations, e.g., 1–10 March against the following 11–20 January,

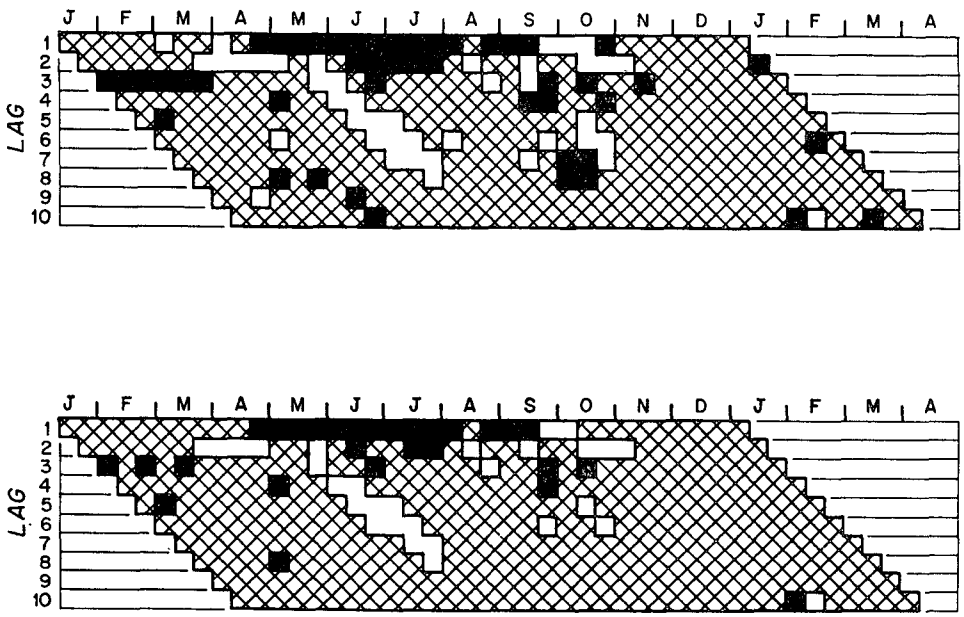

FIG. 10. Lag correlations of 10-day means in 98 years of record. Positively significant correlations are black; negatively significant correlations are white; others are shaded. Significance in the upper diagram is on the 5 per cent level; on the lower it is on the 1 per cent level.

only 98 pairs are available, so for uniformity all correlations were computed for 98 pairs.

Under the null hypothesis that the 36 populations from which the 36 series are drawn are uncorrelated, and that none of the 36 populations is serially correlated (no correlations at lags which are multiples of a year), sample correlation coefficients of 0.19 and 0.26 are significant at the 5 per cent and 1 per cent levels, respectively. Among the 1296 correlations computed however, far more than 5 per cent (or 1 per cent) exceeded 0.19 (or 0.26) in absolute value. The null hypothesis as a whole must, therefore, be rejected.

In view of the arrangement of the data, population correlations at lags of one year can lead to spuriously high sample correlations at shorter lags (Nordö, 1966), but population correlations at shorter lags will not introduce spurious sample correlations at one-year's lag, so that one-year lag correlations may be examined independently of shorter-lag correlations. In contrast to the large total number of significant correlations, there were no more than the expected number of significant correlations at or near one-year's lag. We have not tested for significant correlations at lags of exactly two, three, or more years, but the physical nature of our model renders it unlikely that such correlations would occur in the absence of correlations at one-year's lag. We, therefore, find no reason to reject the latter half of the null hypothesis, and are forced to reject the former half, i.e., to conclude that the correlations at small lags are real. This conclusion becomes all the more plausible when we note that the majority of the significant correlations fall into systematic patterns. Fig. 10 shows the arrangement of significant correlations at lags up to 100 days.

There do not seem to be any systematic relations in late autumn, when the system tends to fluctuate most vigorously. In winter there is some evidence of a positive correlation of 30 days' lag, which may be associated with a preferred period for the large oscillations (the "index cycle"), so evident in Fig. 5. As the preferred period lengthens in spring, a negative correlation appears at 20 days' lag. In late spring a pronounced positive correlation appears at 10 days' lag (it actually reaches 0.76 in July) and extends to 20 days in midsummer. Late April and early May values, however, are negatively correlated with values throughout midsummer. In explanation of the latter pattern, it would appear that a weak temperature gradient in spring would cause the traveling perturbations to die out sooner, thus allowing a stronger temperature gradient to build up by early summer; this gradient will then tend to persist until new wave perturbations develop in autumn. The opposite happens if θ_{01} is large in spring. Further systematic correlations in early autumn may again be associated with preferred periods of the newly developing oscillations.

Even excluding the systematic patterns, the number of significant correlations at lags up to 100 days is somewhat more than expected. This may be a result of sampling, or it may be due to non-zero population correlations at lags of one or more years, which however are too small to verify.

During late fall and winter when our system fluctuates most vigorously and exhibits the greatest amount of variety, it not only shows least evidence of auto-correlation, but it also "forgets" any initial conditions most rapidly. In computing data for the various configurations we started with the first day in January using previously obtained results as initial conditions. We then integrated the system for five years and one month. The first month was not used in the compilation of statistics in order to reduce the possible effect of the initial conditions. Examination showed, however, that the monthly means for the discarded Januaries were not markedly different from those of later Januaries in the same model. The general properties of the initial conditions obviously become irrelevant within a few days. By the same token it seems probable that if any spikes or other short-period random fluctuations were introduced in the forcing function, they would not be discernible in our winter data. In summer, the actual potential temperature θ was seen to follow the equilibrium potential temperature θ^* much more closely. Irregular variations in θ^* during that season would have probably a more obvious influence on the statistical state of the actual atmosphere. Small changes at that time may have also more radical effects on individual circulation patterns.

Acknowledgments. Research by E. B. Kraus is sponsored by the National Science Foundation under Grant GP 317 and by the U. S. Army Electronics Research and Development Laboratory under Contract SC 90784. Research by E. N. Lorenz is sponsored by the Air Force Cambridge Research Laboratories under Contract AF 19(628)-2409.

REFERENCES

Kraus, E. B., and E. N. Lorenz, 1963: A numerical study of the effect of vertical stability on monsoonal and zonal circulations. *Changes of Climate*, UNESCO, 361–372.

Kreuger, A. F., J. S. Winston and D. A. Haines, 1965: Computations of atmospheric energy and its transformation for the northern hemisphere for a recent five-year period. *Mon. Wea. Rev.*, **93**, 227–238.

Lorenz, E. N., 1960: Maximum simplification of the dynamic equations. *Tellus*, **12**, 243.

——, 1965: A study of the predictability of a 28-variable atmospheric model. *Tellus*, **17**, 321–333.

Nordö, J., 1966: Significance of statistical relations derived from geophysical data. *Tellus*, **18** (in press).

Wiin-Nielsen, A., J. A. Brown and M. Drake, 1964: Further studies of energy exchange between the zonal flow and the eddies. *Tellus*, **16**, 168–180.